crystals

MDPI

Article

Numerical Investigation of Ultra-Wide Low-Frequency Wave Attenuation Using Seismic Metamaterials with Auxetic Slender Strips

Haosheng Liu and Hongbo Zhang *

School of Mechanical and Automotive Engineering, Qingdao University of Technology, No 777 Jialingjiang East Road, Qingdao 266520, China; lhsqdlg@qut.edu.cn
* Correspondence: zhbcme1@163.com

Abstract: Seismic metamaterials are an emerging vibration-damping technology, yet concentrating the bandgap in the low-frequency range remains challenging due to the constraints imposed by lattice size. In this study, we numerically investigated seismic metamaterials connected by auxetic (negative Poisson's ratio) slender strips, which exhibit an exceptionally wide low-frequency band gap for vibration isolation. Using a finite element method, we first performed a comparative analysis of several representative seismic metamaterial configurations. The results showed that the auxetic thin strip-connected steel column structure demonstrated outstanding performance, with the first complete band gap starting at 1.61 Hz, ending at 80.40 Hz, spanning a width of 78.79 Hz, and achieving a relative bandwidth of 192.15%. Notably, while most existing designs feature lattice constants in the ten-meter range (with the smallest around two meters), our proposed structure achieves these results with a lattice constant of only one meter. We further analyzed the transmission characteristics of the steel column structure, both with and without concrete filling. Interestingly, significant vibration attenuation, approaching 70 dB, was observed below the first complete band gap (approximately 0.22–1.17 Hz), even without the use of concrete. By comparing the flexural wave band gap with the transmission spectrum, we attributed this attenuation primarily to the presence of the band gap, a phenomenon often overlooked in previous studies. This attenuation at lower frequencies highlights the potential for effectively reducing low-frequency vibration energy. To further enhance the attenuation, the number of periods in the propagation direction can be increased. Additionally, we systematically explored the influence of geometric parameters on the first complete band gap. We found that optimal results were achieved with a slender strip length of 0.05 m, its width between 0.05 and 0.1 m, and a steel structure width of 0.1 m. Our findings underscore the critical role of auxetic thin strips in achieving broadband low-frequency vibration isolation. The approach presented in this study, along with the discovery of low-frequency flexural wave band gaps, provides valuable insights for seismic engineering and other applications requiring effective vibration reduction strategies.

Keywords: auxetic slender strip; ultra-wide low-frequency band gap; seismic metamaterial; lamb wave; flexural wave; finite element method

check for updates

Academic Editor: Luis M. Garcia-Raffi

Received: 11 November 2024
Revised: 18 December 2024
Accepted: 22 December 2024
Published: 26 December 2024

Citation: Liu, H.; Zhang, H. Numerical Investigation of Ultra-Wide Low-Frequency Wave Attenuation Using Seismic Metamaterials with Auxetic Slender Strips. *Crystals* **2025**, *15*, 13. https://doi.org/10.3390/cryst15010013

Copyright: © 2024 by the authors. Licensee MDPI, Basel, Switzerland. This article is an open access article distributed under the terms and conditions of the Creative Commons Attribution (CC BY) license (https://creativecommons.org/licenses/by/4.0/).

1. Introduction

Earthquakes can cause severe casualties and significant property damage. Traditional methods of earthquake disaster prevention have inherent limitations and often fail to adequately protect structures during intense seismic activity. Consequently, there is an

growing demand for innovative disaster mitigation technologies, and the emergence of seismic metamaterials [1–3] presents a promising solution to this challenge.

Metamaterials are sub-wavelength artificial structures that exhibit remarkable properties, such as focusing, super-resolution imaging, stealth, and band gap effects. These characteristics make them widely applicable in fields like optics, acoustics, medicine, thermodynamics, as well as communication and defense [4–6]. This paper mainly focuses on utilizing the band gap properties of metamaterials to control seismic waves. Within the band gap, seismic waves are unable to propagate. Unlike traditional materials, seismic metamaterials suppress wave propagation through the band gap effect, enabling effective attenuation of seismic waves even at extremely low frequencies. These materials hold promise for applications for earthquake-resistant infrastructure, providing an innovative approach to improving the seismic performance of buildings.

Elastic metamaterials can be classified into two types based on the mechanisms that generate band gaps: Bragg scattering and local resonance [7,8]. Bragg-scattering-type metamaterials typically require large sizes to control low-frequency elastic waves because their band gap frequencies are generally proportional to the lattice constant. In contrast, local resonance provides an alternative mechanism for generating band gaps, enabling the control of low-frequency elastic waves with much smaller structures. The resulting band gap can be up to two orders of magnitude smaller than the lattice constant. Most previous research has focused on the isolation effect of seismic metamaterials on surface waves.

In some cases, Lamb waves can also be highly destructive and even dominant [9,10], making it equally important to study the isolation effects of seismic metamaterials on Lamb waves. Du et al. investigated a two-dimensional elastic metamaterial consisting of periodic square concrete-filled steel piles embedded in soil, designed to shield both Lamb waves and surface waves. Their findings indicated that the square pile structure exhibits wider and lower-frequency band gaps compared to cylindrical piles, making it more practical for real-world applications [9]. However, the lattice constants of these materials can reach 10 m, with unit cell heights as large as 20 m, resulting in considerable volume. This design requires significant amounts of steel, leading to high manufacturing costs. Zhang et al. studied the propagation of Lamb waves in a soil medium using seismic metamaterials assembled from periodically arranged cross-shaped and square steel sections. The results showed that there are three complete band gaps (CBGs) below 20 Hz. Seismic metamaterials composed of square steel sections showed superior performance in low-frequency vibration isolation [11]. Luo et al. proposed a new type of seismic metamaterial composed of steel and rubber, designed to attenuate ultra-low-frequency seismic Lamb waves [12]. Notably, they managed to reduce the lattice constant to 2 m and the height to 0.5 m, significantly lowering the material usage, especially steel and rubber, while maintaining excellent vibration isolation performance. Building upon Luo's work, Zhao et al. introduced a coiling structure into seismic metamaterials, utilizing the local resonance mechanism to achieve attenuation effects [13]. Wang et al. proposed a petal-shaped seismic metamaterial that creates ultra-low frequency band gaps by altering the shape of internal scatterers. Their design, validated through numerical simulations and experiments, effectively attenuates seismic waves [14].

The seismic metamaterials mentioned above all utilize materials with a positive Poisson's ratio. Recently, materials with a negative Poisson's ratio (NPR) attracted significant research interest due to their unique properties. Huang et al. designed a simple structure of two-dimensional seismic metamaterials using an NPR material, achieving a wide bandgap that can cover the 2 Hz seismic peak frequency spectrum [15], which primarily causes damage to surface buildings. Li et al. proposed a new type of structure aimed at suppressing seismic waves, particularly low-frequency seismic waves, to protect buildings

from earthquake impacts. This design not only covers the main frequency range of seismic waves but also features a simple structure that is easy to implement, thus showing potential for applications in earthquake engineering [16]. Based on the literature reviewed above, NPR materials have been widely applied in engineering due to their unique properties. However, most existing work focuses on frequencies above 2 Hz. Considering the resonant fundamental frequency of most buildings is mainly concentrated between 1 and 10 Hz, vibration isolation around 1 Hz is also crucial. Although the lattice constant has been reduced to 2 m, seismic metamaterials with smaller dimensions still need further exploration.

In the field of Lamb-wave-type phononic crystal plates, Assouar et al. proposed a mixed phononic crystal plate composed of periodically stepped columns and periodic holes to broaden the acoustic bandgap, achieving a low-frequency wideband sound wave stopband [17]. Coffy et al. introduced a novel design method for phononic crystal strips, providing a detailed theoretical analysis and numerical simulations of their bandgap structure and transmission characteristics [18]. Jin et al. studied a phononic crystal plate with hollow columns connected by slender rods. This connection method can be used to design phononic crystal plates with wider bandgaps [19]. Wang et al. manipulated the guiding of Lamb waves by introducing defects composed of threaded rods and nuts on a perforated solid phononic crystal plate, adjusting the length of the rods to change the resonance frequency of the defects. These studies also offer valuable insights and methods for the research of seismic metamaterials [20].

To address the problems of excessive lattice constant and the difficulty in attenuating seismic waves around 1 Hz, we propose a method combining an NPR material and slender strip structures to achieve efficient attenuation in two distinct frequency ranges: 0.22 Hz to 1.17 Hz (ultra-low frequencies) and 1.61 Hz to 80.40 Hz, with lattice constants of 1 m. Since the frequency of seismic waves typically ranges from 0 to 20 Hz, the broadband attenuation proposed in this paper, covering both ultra-low frequencies and higher frequencies, can effectively shield against seismic waves within the main frequency range. Furthermore, we focus on studying the intrinsic mechanism of vibration isolation in the extremely low frequency range of 0.22 Hz to 1.17 Hz. We introduce the NPR material, and with their simple structural design and high feasibility for mass production, these materials offer enormous potential for applications in the field of earthquake engineering.

The innovations of this paper are summarized as follows: First, it presents a metamaterial connected by thin strips of the NPR material, which can generate band gaps at ultra-low frequencies. Second, it demonstrates vibration isolation in the extremely low frequency range, and its intrinsic mechanism is studied. The approach and the discovery of low-frequency flexural wave band gaps provide valuable insights for seismic engineering and other applications that require effective vibration reduction strategies.

The organization of this paper is as follows: Section 2 introduces the geometric shape and material parameters of the proposed model, along with a brief overview of phononic crystal theory. Section 3 first discusses the band structure and corresponding band gap characteristics of Lamb waves, followed by a frequency-domain analysis of the transmission properties of a two-dimensional periodic structure composed of 6 unit cells. It also conducts a parameter study on the impact of the geometry of NPR foams on seismic performance. Finally, Section 4 summarizes the main findings of this study.

2. Model and Methods

The studied structure with a square lattice is shown in Figure 1, where four slender beams connect a rectangular frame. The lattice constant is denoted as a, and the thickness as h. The length and width of the four beams are represented by l and w, respectively. The outer side length of the rectangular frame is b, and the inner side length is c. The

slender beams can be made from materials such as Plexiglass, Silicon rubber, and NPR foam, depending on the requirements, while the rectangular frame is made of steel. The physical properties of all materials used in this paper are listed in Table 1. These materials are assumed to be isotropic, homogeneous, and linear elastic.

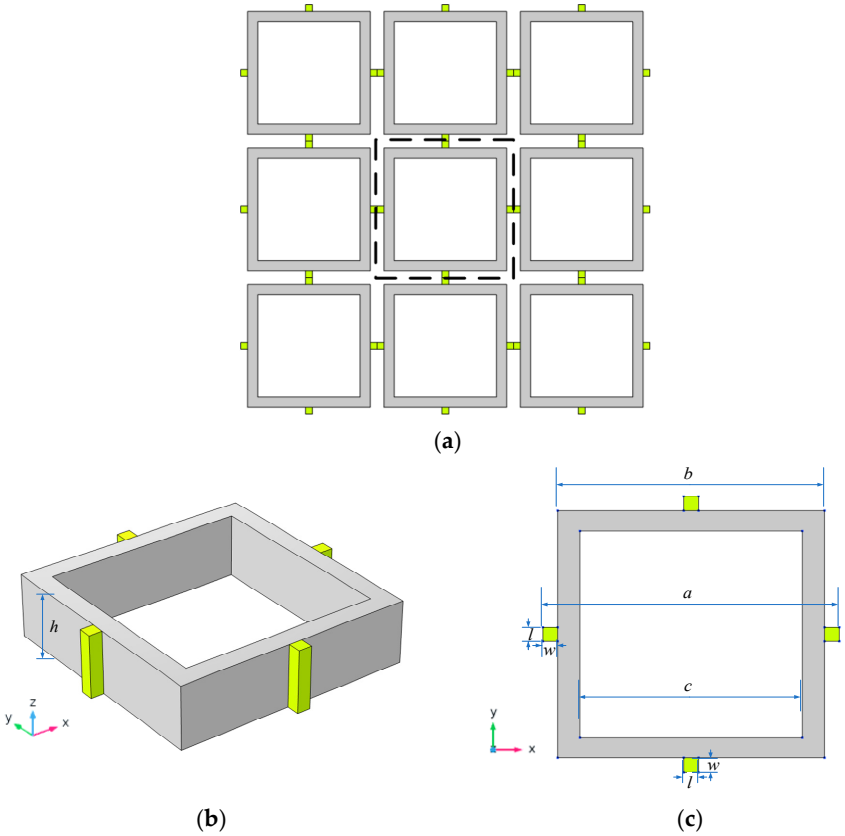


Figure 1. Schematic illustration of the studied structure array and the corresponding unit cell: (**a**) the structure array, (**b**) 3D view of the unit cell, and (**c**) side view showing a square arrangement. The lattice constant is denoted as a and the thickness as h. The length and width of the four beams are represented by l and w, respectively, while the outer and inner side lengths of the rectangular frame are b and c, respectively.

Table 1. The solid material attributes.

Solids	Density (ρ/kg·m^{-3})	Young's Modulus (E/Pa)	Poisson's Ratio (ν)
NPR foam	120	2.5×10^4	-0.8
Steel	7850	207×10^9	0.3
Concrete	2500	40×10^9	0.3
Plexiglass	1142	2×10^9	0.388
Silicon rubber	1300	1.175×10^5	0.4997

The bandgap and transmission characteristics in the frequency domain are analyzed using the finite element method (COMSOL 6.1). The corresponding elastic wave governing Equation can be expressed as follows:

$$\nabla \cdot [C(\mathbf{r}) : \nabla \mathbf{u}] = \rho(\mathbf{r}) \frac{\partial^2 \mathbf{u}}{\partial t^2} \tag{1}$$

where ∇ represents the differential operator; $\mathbf{r}$ is the position vector ($\mathbf{r} = \mathbf{i}x + \mathbf{j}y + \mathbf{k}z$, where $\mathbf{i}$, $\mathbf{j}$, and $\mathbf{k}$ are the unit vectors along the x, y, and z axes, respectively); C represents the elastic

tensor; **u** is the displacement vector; "·" (":") stands for the vector dot product (double-dot product) of two dyadic; ρ represents the density; and t represents time.

Due to the periodicity of the structure, periodic boundary conditions are applied to the connected parts. During meshing, the incident wavelength is discretized into six elements to ensure result convergence. After meshing the unit cell with finite elements, the discrete form of the eigenvalue equation can be written as follows:

$$(\mathbf{K} - \omega^2 \mathbf{M})\mathbf{u} = \mathbf{0} \tag{2}$$

In the Equation, **K** represents the global stiffness matrix, ω is the angular frequency, and **M** represents the global mass matrix.

The COMSOL Solid Mechanics Eigenfrequency Analysis module is used to obtain the band structures. Since the structure under investigation is a two-dimensional plate-like structure, periodic boundary conditions only need to be applied to the connected parts in the x and y directions, therefore:

$$\mathbf{u}(\mathbf{r} + \mathbf{a}) = e^{i(\mathbf{k}\cdot\mathbf{r})}\mathbf{u}(\mathbf{r}) \tag{3}$$

where **r**, **a**, and **k** represent the position vector, the lattice constant vector, and the wave vector, respectively.

The other boundaries are set as free boundary conditions. By sweeping the wave vector **k** over the irreducible Brillouin zone as shown in Figure 2, the band structure can be obtained. The first Brillouin zone and the irreducible Brillouin zone of the two-dimensional periodic plate with a square lattice are shown in Figure 2, where the irreducible Brillouin zone is indicated by the shaded area. A parameterized scan of the wave vector is performed, with a scan range from 0 to 3 and a step size of 1/59, enabling the wave vector to traverse the boundary of the two-dimensional unit cell's first irreducible Brillouin zone, denoted as Γ-X-M-Γ. Finally, the eigenfrequency solver is applied to solve the eigenvalue Equation (3) for each wave vector, as defined in Equation (2).

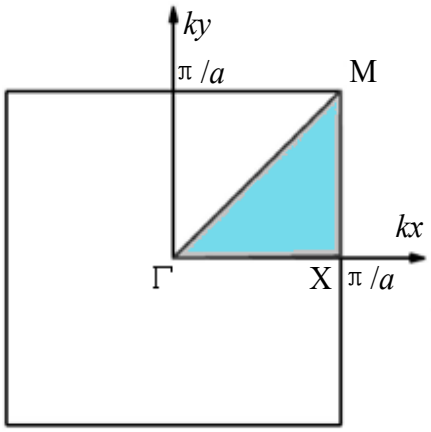


Figure 2. The first Brillouin zone and the irreducible Brillouin zone of the two-dimensional periodic plate with a square lattice, where the irreducible Brillouin zone is indicated by the shaded area.

To quantify the attenuation of vibrations by the bandgap, the transmission characteristics of finite-length metamaterials were studied. The model we established is shown in Figure 3, which consists of a total of 6 unit cells. Perfectly matched layer (PML) boundary conditions are applied on the left and right sides, while periodic boundary conditions are applied on the top and bottom boundaries. The entire region is divided into free tetrahedral meshes, with mesh size controlled by the physical field. A displacement excitation w_{in} is applied perpendicular to the plate surface at the black dot on the left side of the thin plate,

and the displacement response w_{out} is picked up at the black dot on the other side. The transmission loss (TL) is calculated using the following formula:

$$\text{TL} = 20 \log_{10}\left(\frac{w_{in}}{w_{out}}\right) \tag{4}$$

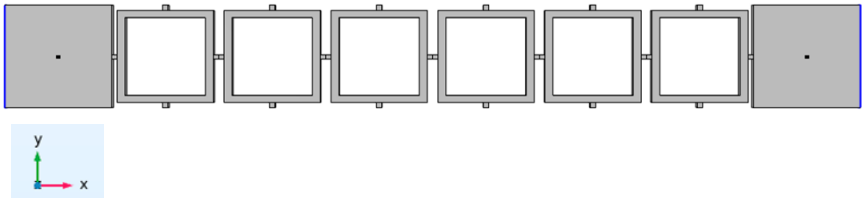


Figure 3. The model we established for the calculation of the TL, which consists of a total of 6 unit cells. PML boundary conditions are applied on the left and right sides, while periodic boundary conditions are applied on the top and bottom boundaries.

3. Results and Discussion

3.1. Band Gap Characteristics of Lamb Waves

To ensure the convergence of the results, 13,377 degrees of freedom (using free tetrahedral mesh) are utilized for the proposed structure in Figure 1. As illustrated in Figure 4, we studied the variation in the frequencies of the upper and lower boundaries of the first complete bandgap with respect to the number of degrees of freedom in the mesh. The results indicate that a good convergence result can be obtained when the number of degrees of freedom is set to 13,377. To further validate our model, the band structures for the structure proposed by Huang et al. [15] are analyzed. The schematic representation of the seismic metamaterial structure is shown in Figure 1a in reference [15]. The used geomitric parameters, material properties, and boundary conditions are the same as those used in Figure 2a in reference [15]. As shown in Figure 5, our results (blue circles) are compared with the results from reference [15] (red dots). It can be observed that our simulated results agree well with those of the reference over the entire frequency range. In particular, both results show that the first band gap ranges from 0.515 Hz to 6.07 Hz, which further validates the present model.

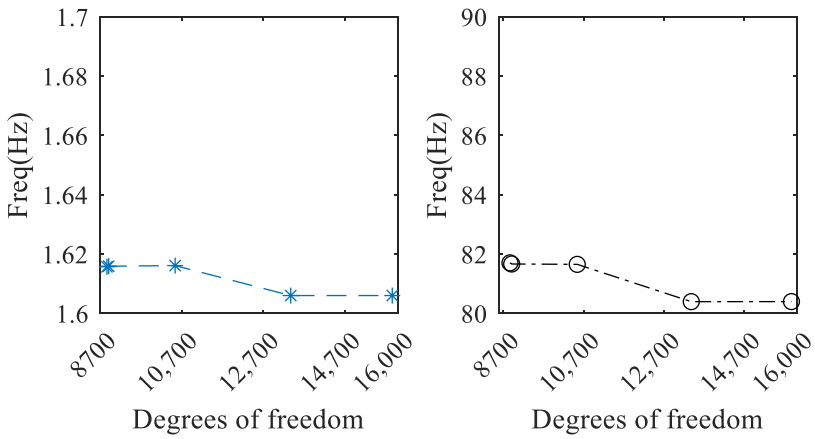


Figure 4. The starting (blue) and cutoff (black) frequencies of the first bandgap as a function of degrees of freedom. As illustrated by the graphs, the frequencies do not vary significantly with further increases beyond 13,377 degrees of freedom. Therefore, the performance of the band gap remains unaffected by mesh quality.

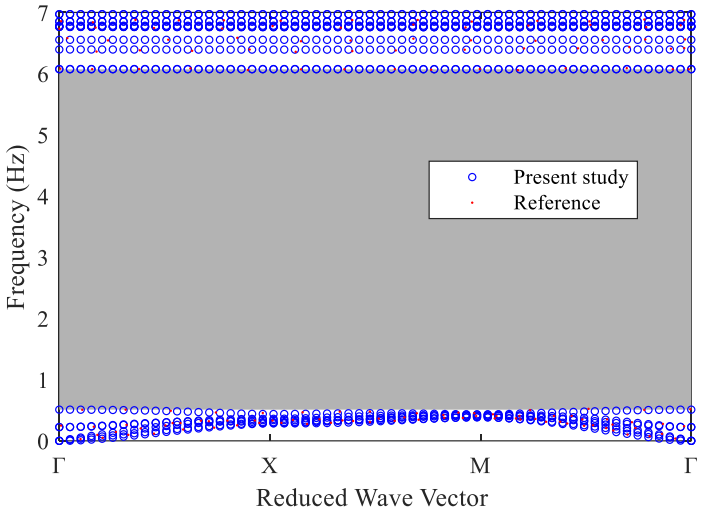


Figure 5. A comparison of the band structures obtained from the current FEM (blue circles) with those obtained by Huang et al. [15] (red dots). Comparing our results with theirs, we can see that our simulated results agree well with theirs over the entire frequency region, thus validating the present model.

We selected several representative seismic metamaterials to highlight the superiority of our negative Poisson's ratio strip-connected metamaterial and to explore the reasons for the superiority of our structure. Figure 6a shows a metamaterial connected by auxetic slender strips, and its geometric parameters are listed in Table 2. We focus only on the first complete bandgap. We define the relative bandwidth of the band gap as $rb = \Delta f / f_c$, where Δf represents the difference between the upper and lower boundaries of the bandgap, and f_c represents the center frequency of the bandgap, calculated as $(f_u + f_l)/2$. f_u (f_l) represents the cutoff (starting) frequency of the bandgap. In this case, the starting frequency of the bandgap is 1.61 Hz, the cutoff frequency is 80.40 Hz, the width of the bandgap is 78.79 Hz, and the relative bandwidth is 192.15%. Figure 6b shows a metamaterial with a traditional configuration, where the width of the outer layer of the NPR material is the same as the width of the slender strips in Figure 1a, both being 0.05 m. All other geometric and material parameters are identical to those in Figure 6a. From Figure 6b, it can be seen that the starting frequency of the first bandgap is 8.32 Hz, the cutoff frequency is 82.42 Hz, the bandgap width is 74.10 Hz, and the relative bandwidth is 163.32%. Compared to the traditional configuration, the bandgap width decreases, but the lower boundary of the bandgap shifts downward, and the relative bandwidth of the bandgap increases by 28.83%. This structure achieves an ultra-wide and ultra-low-frequency bandgap. Compared to the latest studies [15,16], our structure is smaller in size and has a broader relative bandgap. This highlights the advanced nature of our work. More importantly, for seismic waves in the 0–20 Hz range, we have further reduced the control frequency to 1.61 Hz. In Figure 6c, the material of the slender strips was changed to Plexiglass, and no bandgap is observed within the frequency range displayed in the Figure. The starting frequency of its first bandgap is 204.9 Hz, and the cutoff frequency is 252.2 Hz, both of which are well outside the frequency range of interest. When we replaced the slender strip material with silicone rubber, which has a lower Young's modulus, we found that the lower boundary of the first bandgap is 2.13 Hz, the upper boundary is 25.40 Hz, and the bandgap width is 23.27 Hz. Comparing Figure 6a,c,d, for metamaterials connected by slender strips, we can observe that a lower Young's modulus is the primary factor in forming the low-frequency bandgap, while the negative Poisson's ratio contributes to widening the bandgap. In contrast, the influence of density on the bandgap is secondary compared to the effects of Young's modulus and Poisson's ratio.

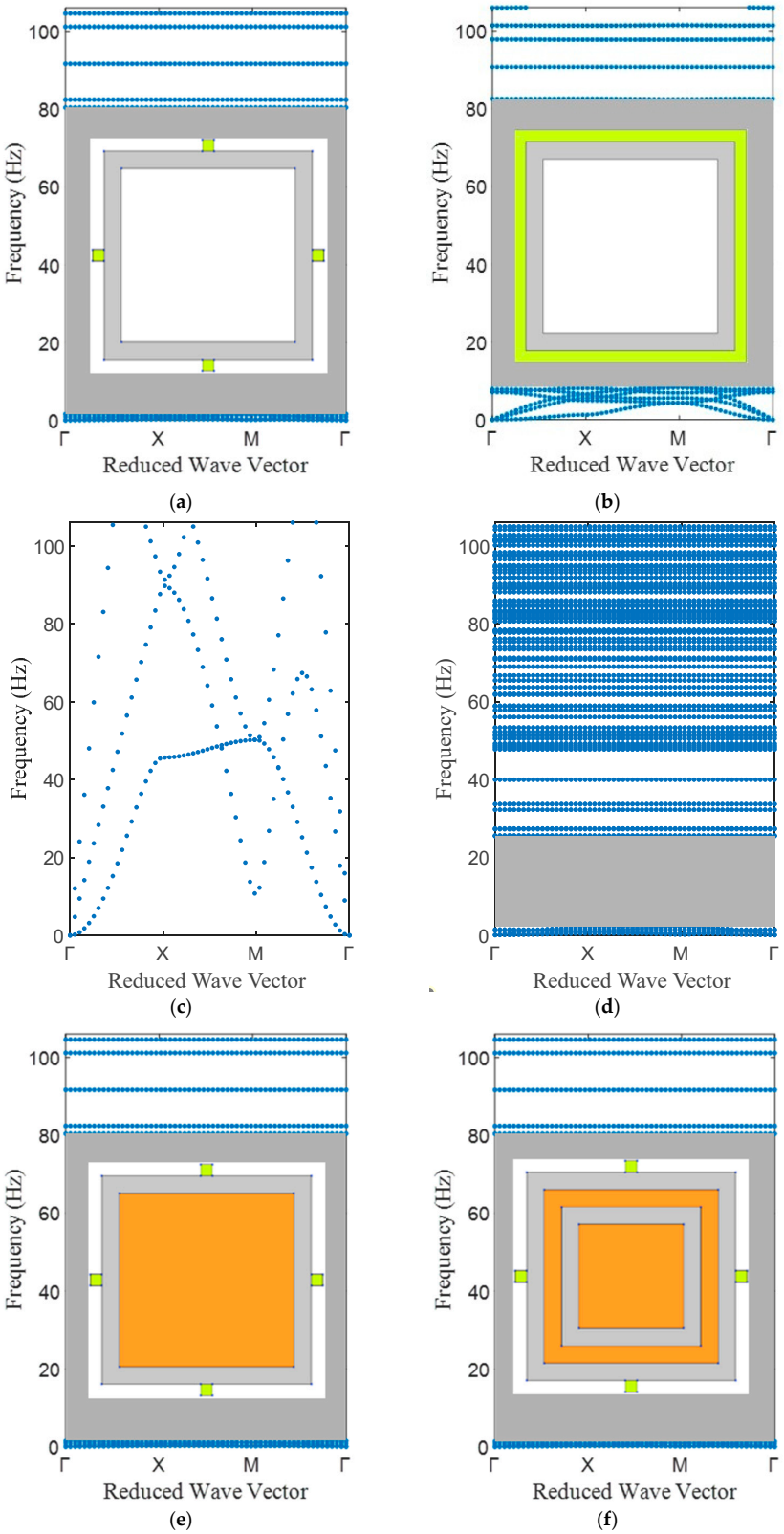


Figure 6. Several representative seismic metamaterials: (**a**) metamaterial connected by NPR foam, (**b**) traditional metamaterial, (**c**) the same structure as (**a**) but with the slender strips made of plexiglass, (**d**) the same structure as (**a**) but with slender strips made of silicone rubber, (**e**) filling the center of the structure in (**a**) with concrete, (**f**) filling the center of the structure in (**a**) with a double-layer steel encapsulation structure. The gray areas or the places indicated by the unit cell in the diagrams represent the locations of complete band gaps. From these diagrams, it can be seen that the structure we propose has the widest band gap and the lowest starting frequency.

Table 2. Geometric parameters of the strip-based metamaterial.

Parameters (m)	***a***	***b***	***c***	***l***	***w***	***h***
Values	1	0.9	0.75	0.05	0.05	0.25

To further reduce the bandgap frequency and expand the bandgap width, we also studied structures with concrete filling in the center of the proposed structure in Figure 1 and a double-layer steel-coated structure. As shown in Figure 6e, the lower boundary of the bandgap is 1.40 Hz, and the upper boundary is 80.40 Hz. For the double-layer steel-coated structure, the lower boundary is 1.31 Hz, with the upper limit remaining at 80.40 Hz. This shows that filling specific structures in the center of the proposed structure can further reduce the lower boundary of the bandgap, but it has little effect on the upper boundary of the bandgap. Next, considering both performance and economic factors, we focus on studying the transmission characteristics of the metamaterial connected by NPR foam to determine the extent to which the first complete bandgap attenuates seismic waves.

3.2. Transmission Characteristics

We focus on studying the transmission characteristics of the proposed metamaterial and the metamaterial filled with concrete. Then, we will identify lower frequency attenuation from the transmission spectrum.

From the energy transmission spectrum in Figure 7, we can observe that the location of energy attenuation aligns well with the position of the bandgap, and two points are worth noting. First, the structure with concrete filling in the center only shows a slight vibration reduction advantage in the range of 40 Hz to 100 Hz. Second, from the zoomed-in view, we can see that, at around 0.22–1.17 Hz, the non-filled structure actually exhibits greater attenuation of seismic waves. However, overall, the difference in seismic wave attenuation between the non-filled and concrete-filled structures is not significant. For the transmission dip with maximum low-frequency attenuation approaching 70 dB, it is necessary to clarify the cause, as our goal is to achieve attenuation at even lower frequencies.

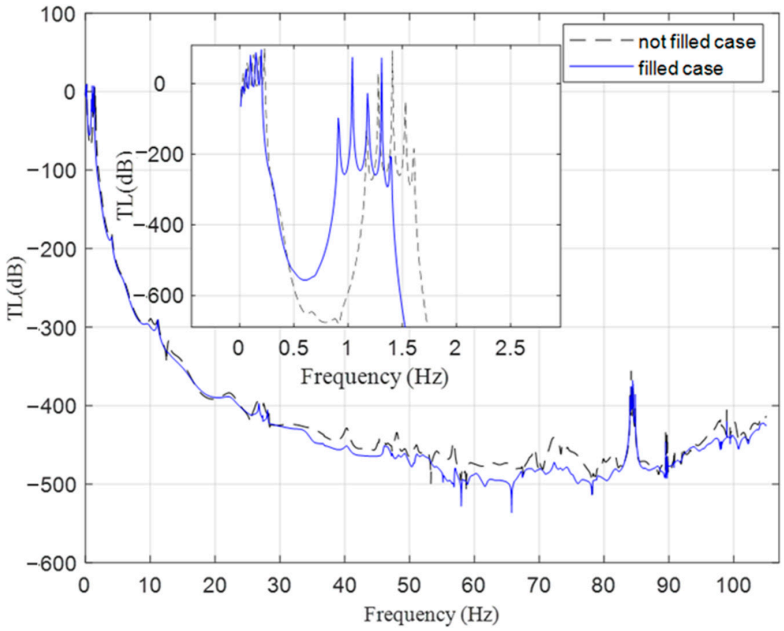


Figure 7. Vibration energy transmission spectra of the slender strip metamaterial and thin strip metamaterial with concrete filling in the center. The inset illustrates the vibration attenuation at extremely low frequencies.

3.3. Bandgap and Transmission Characteristics of Flexural Waves

The flexural wave band structure and transmission spectrum are plotted in Figure 8 for the case in Figure 6a. It can be observed that the flexural wave bandgap in the ΓX direction spans the frequency range from 0.22 Hz to 1.11 Hz. This is generally consistent with the first frequency attenuation range in the transmission spectrum (0.22 Hz to 1.17 Hz). Therefore, we hypothesize that the energy attenuation within this range primarily arises from the directional bandgap in the ΓX direction. As for the broader attenuation range compared to the flexural wave bandgap, one possible reason is that other hybrid modes may also be unable to propagate within this frequency range.

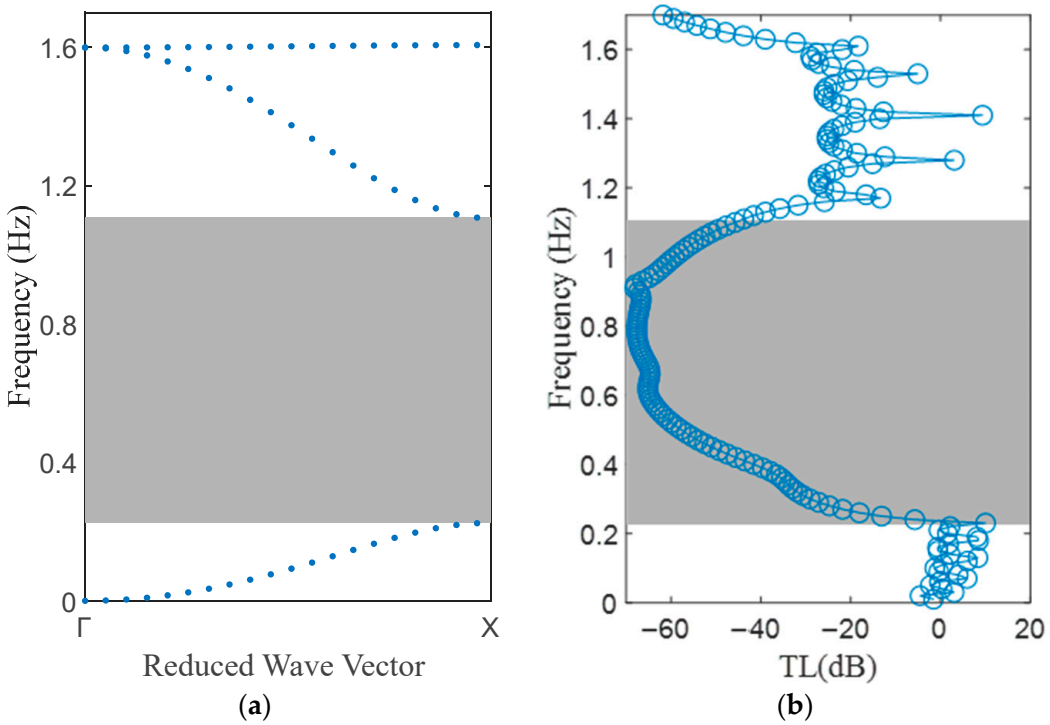


Figure 8. Flexural wave band structure in the ΓX direction (**a**) and its transmission spectrum (**b**). As shown in the diagram, the locations of the directional band gaps and the vibration attenuation largely coincide, confirming that the vibration attenuation is primarily caused by the directional band gaps of flexural waves.

3.4. The Influence of Geometric Parameters on Bandgap Characteristics

3.4.1. The Effect of Slender Strip Width

The widths of the thin strips studied are 0.05 m, 0.1 m, 0.2 m, 0.4 m, and 0.8 m. Figure 9 shows the variation of the upper boundary (f_u), lower boundary (f_l), and central frequency (f_c) of the bandgap. As the width of the slender strips increases, the lower and upper boundaries of the bandgap rise. The upper boundary, however, rises more rapidly, resulting in a larger bandgap. This is not beneficial for low-frequency sound insulation. Furthermore, the bandgap width increases significantly only when the strip width changes from 0.05 m to 0.1 m, while subsequent changes are relatively gradual. Therefore, increasing the width of the slender strip is not advantageous for low-frequency vibration insulation.

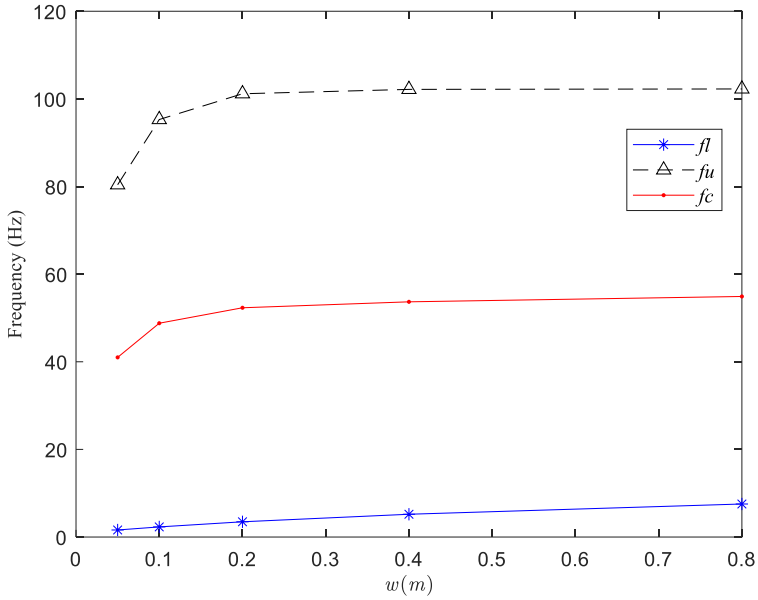


Figure 9. The effect of slender strip width on the first bandgap. As the width of the thin strips increases, both the lower and upper boundaries of the bandgap rise. The upper boundary, however, rises more rapidly, resulting in a larger bandgap. However, this does not benefit low-frequency sound insulation.

3.4.2. The Effect of Slender Strip Length

By changing the length of the thin strips while keeping the lattice constant and the width of the internal steel column unchanged, we can observe the variations in the bandgap. The length ranges from 0.05 to 1 m, with a step size of 0.01 m. As shown in Figure 10, changes in length can significantly affect the position of the bandgap, with both the upper and lower boundaries of the bandgap monotonically decreasing. Moreover, the bandgap width also monotonically decreases, but this is more advantageous for attenuating low-frequency vibrations. Even when the length reaches 0.1 m, the upper boundary remains at 25.70 Hz, which has little effect on the isolation of low-frequency seismic waves.

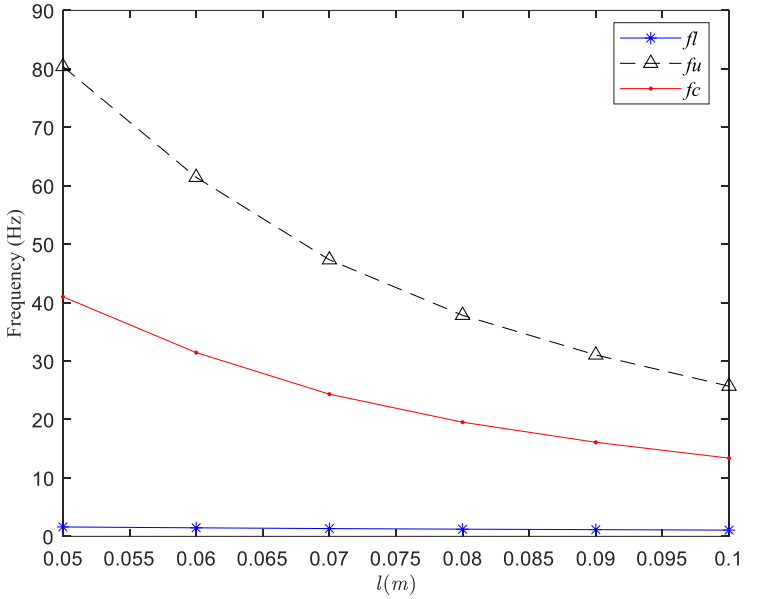


Figure 10. The effect of slender strip length on the first bandgap. As shown in this Figure, changes in length can significantly affect the position of the bandgap, with both the upper and lower boundaries of the bandgap monotonically decreasing.

3.4.3. The Effect of Steel Column Width

With other conditions held constant, the steel column width increases from 0.05 m to 0.25 m, in steps of 0.05 m. The changes in the first complete bandgap are shown in Figure 11. It can be observed that a significant increase in the bandgap occurs only when the width changes from 0.05 m to 1 m, with the upper boundary of the bandgap shifting to higher frequencies and the lower boundary moving downward. However, from 0.1 m to 0.25 m, the lower boundary decreases, while the upper boundary remains essentially unchanged. Therefore, a steel structure width of approximately 0.1 m is found to be the most suitable. Increasing the width of the bandgap is most beneficial for seismic wave insulation.

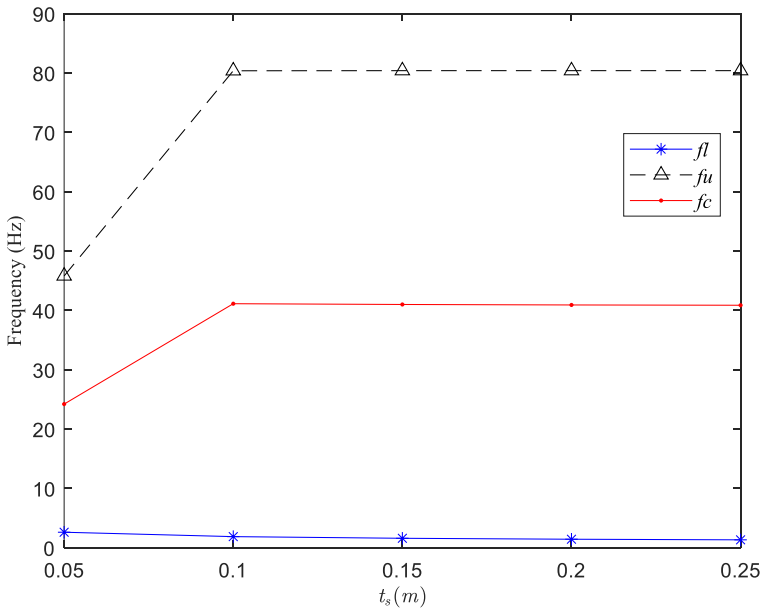


Figure 11. The effect of steel column width on the first band gap. It can be observed that a significant increase in the band gap occurs only when the thickness changes from 0.05 to 1 m, with the upper boundary shifting to higher frequencies and the lower boundary moving downward.

3.5. Discussion and Future Research Plan

We systematically studied the bandgap characteristics and transmission properties of auxetic lattice-connected metamaterials. These metamaterials have been shown to be effective for low-frequency broadband vibration isolation. Special emphasis was placed on investigating the sound insulation properties in the ultra-low-frequency range (0.22–1.17 Hz) and the underlying mechanisms behind their formation. In reference [15], the maximum attenuation in this frequency range is 50 dB, but their lattice constant is ten times larger than ours. In references [12,13], the maximum attenuation in this frequency range is less than 50 dB, and their lattice constant is approximately twice as large as ours. However, it should be noted that although they calculated the transmission loss in this frequency range, they did not conduct an in-depth study of its formation mechanism. The available literature indicates that for conventional buildings, a vibration reduction of 20–40 dB is typically sufficient. For the protection of high-precision instruments, such as MRI equipment in hospitals or laboratory setups, the required isolation performance exceeds 40 dB. High-seismic-performance structures, such as nuclear power plants, bridges, and other critical facilities, may require vibration reduction of 30–50 dB or even higher. It is important to clarify that these values refer to the attenuation of all energy, whereas our focus is specifically on the attenuation of Lamb waves. For the structure we propose, achieving better isolation performance simply requires increasing the number of periods (in our study, we employed six periods).

Our future research aims to design a multifunctional seismic metamaterial [21–24]. First, the seismic metamaterial will integrate carbon nanotubes or similar substances into the NPR material, thereby improving its structural properties [25,26]. Second, we plan to introduce a folded structure to further enhance the attenuation of seismic waves, especially at lower frequencies [27,28]. Third, by applying topology optimization techniques, we aim to improve vibration isolation performance at ultra-low frequencies while simultaneously improving the mechanical properties of seismic metamaterials [29,30]. Fourth, we will leverage cutting-edge manufacturing techniques, such as 3D printing [31,32], to efficiently create high-quality experimental samples. Finally, experiments will be conducted to verify the simulation results. Furthermore, we aim to expand our sensitivity analysis to encompass a broader range of variables. Factors such as boundary conditions, thermal vibrations, scale effects, temperature variations [33], and material inhomogeneity, among others, can have a substantial impact on the performance and reliability of these materials. This expanded sensitivity analysis, drawing from multiple disciplines, will provide a deeper understanding of the robustness and flexibility of material designs. Additionally, it will enhance the accuracy of predicting how these materials will perform in various real-world conditions.

4. Conclusions

We studied seismic metamaterials connected by slender strips with a negative Poisson's ratio using the FEM. By comparing several typical seismic metamaterials, we found that the formation of extremely low-frequency bandgaps of the metamaterial connected by the slender strips is primarily influenced by the small Young's modulus of the slender strips, while the width of the bandgap is mainly influenced by the NPR material. During our investigation of transmission characteristics, we observed a significant low-frequency attenuation around 0.22 Hz to 1.17 Hz. By comparing this with the flexural wave bandgap, we concluded that it is primarily caused by the directional bandgap of flexural waves. We also examined the effects of slender strip width, length, and steel column width on the first bandgap. Our results showed that a slender strip length of 0.05 m, a width between 0.05 and 0.1 m, and a corresponding steel column width of 0.1 m are optimal. The methods presented in this paper and the discovery of low-frequency flexural wave bandgaps provide valuable insights for engineering applications requiring effective vibration reduction strategies, such as seismic resistance.

Author Contributions: H.L.: writing—original draft, investigation, writing—review and editing. H.Z.: conceptualization, formal analysis, supervision, conceptualization, writing—review and editing. All authors have read and agreed to the published version of the manuscript.

Funding: This research was funded by the National Natural Science Foundation of China (Grant No. 12374447 and 11874034) and the Taishan Scholar Program of Shandong (Grant No. ts201712054).

Data Availability Statement: The data are contained within the article.

Acknowledgments: The authors thank Bilong Liu for his assistance in writing and research methodology.

Conflicts of Interest: On behalf of all authors, the corresponding author states that there are no conflicts of interest.

References

1. Wang, Y.; Yang, F.; Yang, J.S.; Tong, L.L.; Liu, Q.; Schmidt, R.; Schröder, K.U. A new priodic seismic metamaterial with ultra-low bandgap for lamb waves. *Mech. Adv. Mater. Struct.* **2023**, *31*, 7742–7752. [CrossRef]
2. Bai, Y.; Li, X.; Zhou, X.; Li, P.; Beer, M. Soil-expended seismic metamaterial with ultralow and wide bandgap. *Mech. Mater.* **2023**, *180*, 104601. [CrossRef]

3. Chen, H.Y.; Qin, Z.H.; Liang, S.N.; Li, X.; Yu, S.Y.; Chen, Y.F. Gradient-index surface acoustic metamaterial for steering omnidirectional ultra-broadband seismic waves. *Extrem. Mech. Lett.* **2023**, *58*, 101949. [CrossRef]
4. Krushynska, A.O.; Janbaz, S.; Oh, J.H.; Wegener, M.; Fang, N.X. Fundamentals and applications of metamaterials: Breaking the limits. *Appl. Phys. Lett.* **2023**, *123*, 240401. [CrossRef]
5. Lu, Q.; Li, X.; Zhang, X.; Lu, M.; Chen, Y. Perspective: Acoustic Metamaterials in Future Engineering. *Engineering* **2022**, *17*, 22–30. [CrossRef]
6. Tzarouchis, D.C.; Koutsoupidou, M.; Sotiriou, I.; Dovelos, K.; Rompolas, D.; Kosmas, P. Electromagnetic metamaterials for biomedical applications: Short review and trends. *EPJ Appl. Metamater.* **2024**, *11*, 7. [CrossRef]
7. Wang, K.; Zhou, J.; Tan, D.; Li, Z.; Lin, Q.; Xu, D. A brief review of metamaterials for opening low-frequency band gaps. *Appl. Math. Mech. Engl.* **2022**, *43*, 1125–1144. [CrossRef]
8. Bae, M.H.; Oh, J.H. Amplitude-induced bandgap: New type of bandgap for nonlinear elastic metamaterials. *J. Mech. Phys. Solids* **2020**, *139*, 103930. [CrossRef]
9. Du, Q.; Zeng, Y.; Huang, G.; Yang, H. Elastic metamaterial-based seismic shield for both Lamb and surface waves. *AIP Adv.* **2017**, *7*, 075015. [CrossRef]
10. Bormann, P.; Engdahl, E.R.; Kind, R. Seismic Wave Propagation and Earth Models. In *New Manual of Seismological Observatory Practice 2 (NMSOP2)*; Deutsches GeoForschungsZentrum GFZ: Potsdam, Germany, 2012; pp. 1–105.
11. Zhang, K.; Luo, J.; Hong, F.; Deng, Z. Seismic metamaterials with cross-like and square steel sections for low-frequency wide band gaps. *Eng. Struct.* **2021**, *232*, 111870. [CrossRef]
12. Luo, Y.M.; Huang, T.T.; Zhang, Y.; Xu, Y.Y.; Xie, Y.M.; Ren, X. Novel meter-scale seismic metamaterial with low-frequency wide bandgap for Lamb waves. *Eng. Struct.* **2023**, *275*, 115321. [CrossRef]
13. Zhao, C.; Chen, Q.; Wang, Y. Low-Frequency Band Gap Seismic Metamaterials for Lamb Wave Based on Vibration-Sensitive Scatterers. *J. Vib. Eng. Technol.* **2024**, *12*, 7903–7915. [CrossRef]
14. Wang, Y.; Yang, F.; Yang, J.S.; Tong, L.L.; Li, S.; Liu, Q.; Hou, G.L.; Sun, P.D.; Xing, M.; Zheng, G. Study on vibration damping performance of a petal-shaped seismic metamaterial. *Structures* **2023**, *56*, 104898. [CrossRef]
15. Huang, T.T.; Ren, X.; Zeng, Y.; Zhang, Y.; Luo, C.; Zhang, X.Y.; Xie, Y.M. Based on auxetic foam: A novel type of seismic metamaterial for Lamb waves. *Eng. Struct.* **2021**, *246*, 112976. [CrossRef]
16. Li, P.; Yang, F.; Zhao, M.; Du, Z.; Fan, H. A new seismic metamaterial design with ultra-wide low-frequency wave suppression band utilizing negative Poisson's ratio material. *Eng. Struct.* **2024**, *319*, 118821. [CrossRef]
17. Badreddine Assouar, M.; Sun, J.H.; Lin, F.S.; Hsu, J.C. Hybrid phononic crystal plates for lowering and widening acoustic band gaps. *Ultrasonics* **2014**, *54*, 2159–2164. [CrossRef] [PubMed]
18. Coffy, E.; Lavergne, T.; Addouche, M.; Euphrasie, S.; Vairac, P.; Khelif, A. Ultra-wide acoustic band gaps in pillar-based phononic crystal strips. *J. Appl. Phys.* **2015**, *118*, 214902. [CrossRef]
19. Jin, Y.; Pennec, Y.; Pan, Y.; Djafari-Rouhani, B. Phononic crystal plate with hollow pillars connected by thin bars. *J. Phys. D Appl. Phys.* **2017**, *50*, 035301. [CrossRef]
20. Wang, Y.F.; Yang, L.; Wang, T.T.; Chen, A.L.; Laude, V.; Wang, Y.S. Guided Lamb waves in reconfigurable phononic crystal waveguides. *APL Mater.* **2021**, *9*, 081110. [CrossRef]
21. Ning, L.; Wen, P.H. Design of a multifunctional elastic wave metamaterial for detecting or hiding objects. *Appl. Math. Model.* **2024**, *132*, 211–225. [CrossRef]
22. Xu, J.; Song, X.; Zhao, B.Y.; Yang, H.J.; Sui, D.; Zhou, J.; Xiao, H. 3D-printed multifunctional chiral metamaterial with invariant sound absorption under large deformation and low-frequency vibration control. *Virtual Phys. Prototyp.* **2024**, *19*, e2425386. [CrossRef]
23. Ghandehari, M.A.; Masoodi, A.R. Inherent resonance of carbon and graphene-based nanocomposite coupled single-span arch beams. *Compos. Part C-Open* **2024**, *14*, 100458. [CrossRef]
24. Zhang, Q.; Sun, Y. Low frequency bandgap and high stiffness of innovative auxetic metamaterial with negative thermal expansion. *Thin Wall. Struct.* **2024**, *201*, 112010. [CrossRef]
25. Shen, J.; Wang, Y.; Yu, Y.; Fu, P.; Zhang, M.; Qing, L.; Yang, Y. Hybrid effects of carbon nanotubes and nano-rubber on the mechanical properties and microstructure of oil well cement paste cured at different temperatures: Experimental studies and a micromechanical model. *Cem. Concr. Compos.* **2025**, *156*, 105842. [CrossRef]
26. De, B.; Bera, M.; Bhattacharjee, D.; Ray, B.C.; Mukherjee, S. A comprehensive review on fiber-reinforced polymer composites: Raw materials to applications, recycling, and waste management. *Prog. Mater. Sci.* **2024**, *146*, 101326. [CrossRef]
27. Liu, J.; Zeng, T.; Ni, H.; Hou, Y.; Pan, G. A new local resonance metamaterial for flat and cylindrical structures depended on elastic chiral spiral beams. *Sci. China Technol. Sci.* **2024**, *67*, 3597–3611. [CrossRef]
28. Chen, K.; Dong, X.; Peng, Z.; Meng, G. Reconfigurable topological gradient metamaterials and potential applications. *Thin Wall. Struct.* **2024**, *205*, 112572. [CrossRef]

29. Yin, S.; Huang, J.; Liu, S.; Gu, S.; Bui, T.Q.; Zhao, Z. Isogeometric topology optimization for maximizing band gap of two-dimensional phononic crystal structures. *Appl. Math. Model.* **2025**, *137*, 115702. [CrossRef]
30. Liao, L.; Yao, S.; Li, Y. Topological optimization design of multi-material phononic crystals with floating projection constraints to achieve ultra-wide band gap. *Compos. Struct.* **2024**, *346*, 118387. [CrossRef]
31. Zhou, J.; Lun, Y.; Zhao, Y.; Lei, H.; Lei, Y.; Wei, K.; Hou, Z.; Hong, J. Strain-independent auxetic metamaterials inspired from atomic lattice. *Int. J. Mech. Sci.* **2024**, *281*, 109614. [CrossRef]
32. Guo, J.C.; Li, J.R.; Wang, H.Y.; Dong, Z.Y.; Zhang, Z. High strength induced wide band gap formations in additively manufactured cubic metamaterial. *Smart Mater. Struct.* **2024**, *33*, 075019. [CrossRef]
33. Ghandehari Moein, A.; Masoodi Amir, R. Employing GDQ method for exploring undamped vibrational performance of CNT-reinforced porous coupled curved beam. *Adv. Nano Res.* **2023**, *15*, 551–565.

Disclaimer/Publisher's Note: The statements, opinions and data contained in all publications are solely those of the individual author(s) and contributor(s) and not of MDPI and/or the editor(s). MDPI and/or the editor(s) disclaim responsibility for any injury to people or property resulting from any ideas, methods, instructions or products referred to in the content.